

Radiative Instabilities in Simulations of Spherically Symmetric Supernova Blast Waves

Paul A. Kimoto

Department of Physics, Cornell University, Ithaca, NY 14853

and

David F. Chernoff

Department of Astronomy, Cornell University, Ithaca, NY 14853

accepted by The Astrophysical Journal
©1997 The American Astronomical Society

ABSTRACT

High-resolution simulations of the cooling regions of spherically symmetric supernova remnants demonstrate a strong radiative instability. This instability, whose presence is dependent on the shock velocity, causes large-amplitude fluctuations in the shock velocity. The fluctuations begin almost immediately after the radiative phase begins (upon shell formation) if the shock velocity lies in the unstable range; they last until the shock slows to speeds less than approximately 130 km s^{-1} . We find that shock-velocity fluctuations from the reverberations of waves within the remnant are small compared to those due to the instability. Further, we find (in plane-parallel simulations) that advected inhomogeneities from the external medium do not interfere with the qualitative nature of the instability-driven fluctuations. Large-amplitude inhomogeneities may alter the phases of shock-velocity fluctuations, but do not substantially reduce their amplitudes.

Subject headings: hydrodynamics—instabilities—shock waves—ISM: supernova remnants

1. Introduction

The simplest description of a supernova remnant involves a spherically symmetric shell whose expansion is smoothly decelerated by the surrounding interstellar medium. Actual remnants appear irregular, and this description must be supplemented by considering a variety of physical effects (Chevalier 1977; Draine & McKee 1993). Among the instabilities that have been investigated are convective motions, the rippling of thin dense shells, and cooling instabilities affecting radiative shocks.

Much work has been done to investigate instabilities that may arise during the initial interactions between a supernova and its surrounding medium, during which the supernova first begins to decelerate. Included are convective Rayleigh-Taylor-type instabilities in hollowed-out Sedov-Taylor solutions (Goodman 1990) and at the interface between shocked supernova gas and shocked gas from the surroundings (Chevalier, Blondin, & Emmering 1992; Chevalier & Blondin 1995), and the effects of expansion into material with exponentially decreasing density (Luo & Chevalier 1994). These instabilities do not prevent the blast wave from entering an adiabatic phase roughly described by the standard Sedov-Taylor solution.

The dense shell that forms much later, when a remnant enters the radiative phase (in which the cooling timescale becomes shorter than the remnant age) is subject to a rippling instability (Vishniac 1983; Bertschinger 1986). When it occurs, the deviations from sphericity oscillate overstably, and the shell becomes wrinkled. Linear models indicate that the oscillations grow as a power law in time.

This paper focuses on the effects of the global cooling overstability on the evolution of a spherically symmetric supernova remnant. In this instability the cooling lengths of radiative shocks oscillate (Langer, Chanmugam, & Shaviv 1981; Chevalier & Imamura 1982; Imamura, Wolff, & Durisen 1984). The phenomenon is essentially one dimensional, in the direction of shock propagation, and so is easily amenable to numerical investigation. The instability develops exponentially rapidly, and (in the context of a decelerating shock) requires no other external perturbations. Bertschinger (1986) suggested that this cooling instability could provide the initial seed perturbations to drive the slower-growing, later-phase rippling instability.

According to linear perturbative analysis with power-law cooling laws $\mathcal{L} \propto \rho^2 T^\alpha$, instability occurs when α is small, $\alpha \lesssim 0.8$ (Chevalier & Imamura 1982). With such cooling laws, fast shocks support long cooling lengths, and slow shocks require short cooling lengths. Deviations from steady-state flow tend to drive the system away from that steady state.

Innes, Giddings, & Falle (1987) and Gaetz, Edgar, & Chevalier (1988) studied the evolution of plane-parallel shocks with nonequilibrium cooling processes. The simulations, which included the history-dependent effects of nonequilibrium cooling, showed that shocks with mean velocities $v_s \gtrsim 130 \text{ km s}^{-1}$ are unstable. Observations of the Vela supernova remnant (Raymond, Wallenstein, & Balick 1991) have found evidence consistent with the presence of unsteady flow like that produced by this instability—unusually broad line widths (of Si II and Mg II) and a discrepancy between the shock ram pressure and the postshock thermal pressure.

Cioffi, McKee, & Bertschinger (1988) gave a global picture of the evolution of a spherically symmetric supernova remnant. Although this treatment of the entire remnant interior over most of the life of the remnant was not concerned with the details of shell formation, its supernova models provide a context for studying the instability.

In the calculations we discuss below, like Cioffi et al. (1988) we simulate a 0.931×10^{51} ergs explosion into a spherically symmetric interstellar medium. We adopt a simple cooling

law $\mathcal{L} = n_{\text{H}}^2 f(T)$, where n_{H} is the density of hydrogen nuclei and $f(T)$ is a piecewise power-law fit to the results of Raymond, Cox, & Smith (1976), altered to turn off at low temperatures (cf. Appendix A). We assume the gas to be completely ionized, and to include helium in a 1:10 ratio to hydrogen. This cooling law should allow us to capture the features of the cooling that lead to oscillations of the cooling column.

When the remnant is young, the gas is hot, the cooling rate is small, and so the remnant is roughly adiabatic. The remnant changes from adiabatic to radiative near the time at which the remnant age equals the cooling time of the gas at the shock front. When cooling sets in, the gas behind the shock loses pressure support and so (1) the shock speed drops suddenly and (2) a dense shell builds up behind the shock. Between the shock and the dense shell lies the cooling region.

After a brief transition period, the behavior of the shock position r_s changes from the adiabatic scaling $r \propto t^{2/5}$ toward the “pressure-driven snowplow” scaling $r \propto t^{2/7}$ (Cioffi et al. 1988). Since the timescale of the dynamical cooling instability is comparable to the cooling time (Chevalier & Imamura 1982), the effects of the instability appear at the onset of the radiative phase if the shock velocity is sufficiently high (i.e., if allowed by the cooling law at the shock temperature). The shock oscillations persist until the shock speed becomes too slow.

Analytic estimates by Cioffi et al. (1988) give the time of shell formation as

$$t_{\text{sf}} = 3.61 \times 10^4 E_{51}^{3/14} n_{\text{H},1}^{-4/7} \text{ yr}, \quad (1)$$

where E_{51} is the initial explosion energy in units of 10^{51} ergs, $n_{\text{H},1}$ is the interstellar density in units of 1 cm^{-3} , and we assume that the metallicity is given by solar abundances. During shell formation the shock velocity drops strongly until some postshock gas ends its period of rapid cooling, at which time this gas reaches its greatest density. Then the shock begins to move with the dense shell in the pressure-driven snowplow stage. The shock radius and velocity tend toward

$$R_s = 14 E_{51}^{2/7} n_{\text{H},1}^{-3/7} \left(\frac{4e}{3} \frac{t}{t_{\text{sf}}} - \frac{1}{3} \right)^{3/10} \text{ pc}, \quad (2)$$

$$v_s = 413 n_{\text{H},1}^{1/7} E_{51}^{1/14} \left(\frac{4e}{3} \frac{t}{t_{\text{sf}}} - \frac{1}{3} \right)^{-7/10} \text{ km s}^{-1} \quad (3)$$

(Cioffi et al. argue that these offset power laws are better estimates than the familiar power-law relations).

The possibility for oscillations begins at this time. In our simulations we find that this stage begins near the time $1.4 t_{\text{sf}}$. In order to have oscillations, the shock velocity must exceed some cutoff value v_c . Adopting the approximate expression (3) for v_s during this stage (which, however, appears to be an overestimate at such early portions of this stage), we obtain the requirement

$$n_{\text{H},1}^2 E_{51} \gtrsim 0.39 \left(\frac{v_c}{130 \text{ km s}^{-1}} \right)^{14}. \quad (4)$$

The oscillations may begin immediately upon shell formation (as they do in all of our simulations with oscillations) and last until the shock velocity drops to v_c at

$$t_c \approx t_{\text{sf}} \left[0.09 + 1.44 \left(\frac{v_c}{130 \text{ km s}^{-1}} \right)^{-10/7} n_{\text{H},1}^{10/49} E_{51}^{5/49} \right]. \quad (5)$$

The oscillation period is approximately $2\pi t_{\text{cool}}$, where t_{cool} is given by the cooling rate at the shock temperature (Chevalier & Imamura 1982). Since this cooling time drops rapidly as the shock slows, typically many cycles occur before the oscillations cease.

The approximate expression (2) for shock radius R_s during the pressure-driven snowplow stage gives the corresponding bounds on shock radii for which oscillations may occur. The intervals in time and shock radius are shown in Figure 1, where the two lines represent the approximate beginning and end of the intervals. (We adopt $v_c = 130 \text{ km s}^{-1}$ for this simple illustration.) The need for sufficiently high shock velocity at the time of shell formation (4) is reflected by the truncation of this region at low values of n_{H} .

(As noted, the shock velocity is the criterion for determining whether the shock motion is stable. With a cooling term of the form $\rho^2 f(T)$ [as we employ], solutions to the equations of motion are invariant under the transformation $\rho \rightarrow A\rho$, $p \rightarrow Ap$, $E \rightarrow E/A^2$, $t \rightarrow t/A$, $r \rightarrow r/A$. As long as we can neglect the details of the initial explosion, we can cover the range of values of explosion energy E_{51} by varying the interstellar-medium density n_{H} , and applying this transformation. The axes in Figure 1 are labeled to reflect this convenient result.)

2. Numerical simulations of shock-velocity oscillations

All of our spherically symmetric calculations assume an explosion energy of 0.931×10^{51} ergs. Our inflowing gas has a temperature $T_{\text{in}} = 2500 \text{ K}$. This is of course unrealistic, but the particular value does not affect the evolution of the shock so long as the shock remains strong. The rarest medium we consider has a density $n_{\text{H}} = 0.1 \text{ cm}^{-3}$. In the course of the simulations discussed below, the shock velocity becomes as low as 49 km s^{-1} , with a Mach number of 6.5. For such a interstellar-medium phase, however, one expects the interstellar medium to have $T_{\text{ISM}} \approx 10000 \text{ K}$. A 49 km s^{-1} shock expanding into this hotter medium has a modest Mach number of 3.3, but the postshock compression is just 20% greater than the case of our 2500 K medium. For larger-density interstellar-medium phases one expects ambient temperatures less than 2500 K and smaller discrepancies in the postshock compression. In these cases the fact that shocks faster than 110 km s^{-1} heat preshock gas to temperatures $T_{\text{in}} \sim 10000\text{--}30000 \text{ K}$ (Shull & McKee 1979) limits the shock strength. We find that the maximum deviation in the postshock compression is less than 15% from our numerical case.

The cooling law $\mathcal{L} = n_{\text{H}}^2 f(T)$ uses for the cooling function $f(T)$ a piecewise power-law fit to the result presented by Raymond et al. (1976), as discussed above. To account crudely for the turnoff

of cooling in the recombination zone behind the shock front, we arrange for the cooling to vanish below a cutoff temperature $T_c \approx 2 \times 10^4$ K. Our use of this function assumes that the emitting plasma is in collisional equilibrium. Because collisional, ionization, and recombination rates are slow compared to the cooling rate, the evolution of the ionization state lags our equilibrium assumption (Innes et al. 1987; Gaetz et al. 1988). At shock speeds greater than 110 km s^{-1} , photons emitted by hot postshock gas preionize the inflowing gas (Shull & McKee 1979) so that the postshock gas tends to evolve toward equilibrium, but at lower shock speeds, where preionization is not so complete, postshock ionization rates are slow and the cooling may differ greatly from our equilibrium assumption. nonequilibrium simulations (Innes et al. 1987; Gaetz et al. 1988) indicate that oscillations occur for shock speeds $\gtrsim 130 \text{ km s}^{-1}$ and that the essential feature required is a cooling law with a small local power-law index α . Our equilibrium law should capture the correct qualitative behavior because it has this feature. With a more realistic cooling law, requiring explicit evolution of the ionization, simulating the many oscillations shown below would be a much more computationally taxing task. Using our simplified cooling law our longest simulation (the high-density $n_{\text{H}} = 50 \text{ cm}^{-3}$ case) required approximately six days of computing on a Sun Sparc 10 workstation.

Since we are interested in the dynamics of the cooling region (unlike, for example, Cioffi et al. [1988]), our numerical simulations must allow for high resolution between the shock front and the dense shell. The cooling length L_{cool} is quite short compared with the remnant radius, and as the dense shell expands and slows, the disparity between these two length scales increases. Our Eulerian finite-difference method incorporates a hierarchy of grids that allows high-resolution subgrids to be placed where needed. We place high-resolution subgrids in the cooling region; typically on the order of 100 grid points (evenly spaced, for the average cooling length) are required to resolve the dynamics that drive the oscillatory instability. In cases where the disparity between cooling length and remnant size is the greatest (that is, at the lowest speeds for which instability is expected), we find that it is sufficient to place such high resolution at the two ends of the cooling region (the shock front and the transition to the cool, dense shell), which have the steepest gradients. (Appendix A describes the model and numerical methods in more detail.) Unfortunately, even at this level of resolution, it is possible to validate the results of the simulations with rigorous convergence tests (e.g., Kimoto & Chernoff 1995) only for short time intervals. Experimentation with simulations with different resolutions indicates, however, that (1) we are able to identify when the instability is and is not present, and (2) we can readily determine the relative amplitudes and periods of oscillation to $\lesssim 10\%$.

For simplicity we simulate only a portion of the remnant’s interior. For our first cases we start the simulations at an age well within the remnant’s adiabatic phase, with the exact Sedov-Taylor blast-wave solution for adiabatic, point-like explosions (Sedov 1959). For an interior boundary condition we set the flow variables equal to the values given by the Sedov-Taylor solution. We impose this condition at a radius small enough so that it has no effect on the evolution of the region close to the shock.

In Figures 2, 3, and 4 we show the evolution of the shock position r_s and shock speed v_s for three choices of the interstellar medium density. The lowest value, $n_H = 0.1 \text{ cm}^{-3}$, is the value used by Cioffi et al. (1988). The other two values, $n_H = 5.5$ and 50 cm^{-3} , are chosen so that their shock temperatures at the time of shell formation lie in different power-law regions of our cooling law: the power-law index changes from $\alpha \approx -2.2$ to $\alpha \approx -0.1$ at $T = 5 \times 10^5 \text{ K}$, corresponding to a shock velocity of 190 km s^{-1} . For the $n_H = 0.1 \text{ cm}^{-3}$ simulation shown we use over the bulk of the remnant a grid size $\Delta r = 0.0064 \text{ pc}$ ($\Delta r/r_s \approx 0.012\%$), and in the neighborhood of the shock, a smaller grid size $\Delta r = 0.0008 \text{ pc}$ (a factor of 8 smaller). The interior computational boundary, at which the Sedov-Taylor solution is imposed, is at $r = 31 \text{ pc}$. For the $n_H = 5.5 \text{ cm}^{-3}$ simulation, we use $\Delta r = 0.0016 \text{ pc}$ ($\Delta r/r_s \approx 0.014\%$) over the bulk of the remnant, and on the cooling region Δr varies from 0.0001 pc to 0.00005 pc as necessary to maintain $\Delta r/L_{\text{cool}} \approx 1\%$. (In addition a grid with $\Delta r = 0.000025 \text{ pc}$ covers the shock neighborhood.) The interior boundary is at $r = 4.1 \text{ pc}$. For the $n_H = 50 \text{ cm}^{-3}$ simulation, $\Delta r = .001 \text{ pc}$ ($\Delta r/r_s \approx 0.02\%$) over the bulk of the remnant, and on the cooling region Δr varies from 0.00013 pc to 0.000016 pc as necessary to keep $\Delta r/L_{\text{cool}} \approx 1\%$. (Throughout the shock is resolved by a grid with $\Delta r = 0.000004 \text{ pc}$.) The interior boundary is at $r = 1.5 \text{ pc}$.

In all cases, the shock velocity changes significantly at the time of shell formation. In the case of the rarest medium, after the dense shell forms, the shock velocity ($v_s \approx 90 \text{ km s}^{-1}$) is too low for oscillations to begin. In the other two cases there are many oscillations before the instability subsides, near $v_s \approx 120 \text{ km s}^{-1}$. The $n_H = 50 \text{ cm}^{-3}$ simulation shown in Figure 4 extends until we lose sufficient resolution to determine the oscillation amplitude to within 10%; however, we still can continue the evolution to determine for how long the instability persists. (The region of the cooling law with power-law index $\alpha \approx -2.2$ terminates at a temperature corresponding to a shock velocity $v_s = 130 \text{ km s}^{-1}$. The difference between our cutoff value and that of Innes et al. [1987] and of Gaetz et al. [1988] is due to the different cooling treatment that we adopt. The slope of our less realistic piecewise power-law cooling law supports oscillations at lower temperatures.) The amplitudes of the oscillations in v_s are quite large; they lie in a nonlinear regime in which the amplitudes have reached a saturation value. The amplitudes do not appear to depend on the different power laws in the cooling function. We note that the oscillations do not affect the gross behavior of r_s as a function of time.

To assess the physical significance of this particular mechanism for producing fluctuations in the shock velocity, we next consider several other physical mechanisms for producing shock-velocity fluctuations.

First we discuss the effect of “reverberations” on the shock velocity. The birth of the remnant leaves behind waves that propagate back and forth inside the remnant. To investigate the evolution of these waves, we must adopt somewhat more realistic initial and interior-boundary conditions. Following Cioffi et al. (1988), for a revised initial condition we begin at a time close to the explosion, placing the explosion kinetic energy into a ball with constant density (100 times the ISM density) and fixed total mass ($3 M_\odot$). We set the velocity distribution to be linear with radius,

$v \propto r$, as might be expected for a collection of particles that have not yet interacted appreciably with the surrounding cold medium. The pressure in the ball is set to the ISM value. (The total thermal energy in the ball is essentially negligible, over eight orders of magnitude smaller than the total kinetic energy.) For an interior boundary condition, we choose a “hard-sphere,” perfectly reflecting boundary at the small radius $r_{\text{inner}} = 0.25 \text{ pc}$.

Figure 5 shows the resulting time evolution of v_s for the case of the low-density interstellar medium ($n_{\text{H}} = 0.1 \text{ cm}^{-3}$). (This simulation uses $\Delta r = 0.01 \text{ pc}$; in the period shown the shock radius expands to 66 pc.) Well after the mass swept up exceeds the initial explosion mass, only occasional, small-amplitude fluctuations perturb the overall evolution of the shock velocity. Other deviations from the smooth evolution of v_s are similar to those seen in the simulations without the violent initial conditions (in Figure 2).

Figure 6 shows the mass density, velocity, and pressure of the flow at a remnant age of $5 \times 10^4 \text{ yr}$, well before the shell-formation time. In the remnant interior the most apparent differences from the smooth Sedov-Taylor solution (shown with dotted lines) are (1) inward flow near the center of the remnant, (2) a density enhancement (at the arrow in the top panel) formed when the shock developed, and (3) a weak shock (at the arrow in the bottom panel) traveling toward the main shock. The small v_s fluctuation in Figure 5 at $t \approx 1.2 \times 10^5 \text{ yr}$ occurs when the weak shock reaches the main shock. Although other waves in the remnant interior may travel between these features and the main shock and perturb the progress of the main shock, none have appreciable amplitude. We conclude that the effect of reverberations on the evolution of the shock front must be small, particularly in comparison with the effects of the radiative instability. In our simulations such waves may decay in part because of insufficient numerical resolution, but it is unlikely that they would cause substantial variation in v_s . Some differences from the flows shown in Cioffi et al. (1988) may arise from differences in initial conditions.

As a second source of possible shock-velocity fluctuations, we consider density fluctuations in the upstream gas. Here we perform simulations in the simpler plane-parallel geometry. The cold gas flows into the computational region from the upstream boundary into the shock and then into the cooling region. This structure ends at a wall at the other boundary. As discussed at the end of §1, because our cooling law has the form $\mathcal{L} \propto \rho^2 f(T)$, for each inflow velocity it suffices to consider just one value of the inflow (interstellar) density, and we arbitrarily choose $n_{\text{H}} = 50 \text{ cm}^{-3}$. For a given mean shock velocity and upstream temperature, we can then convert to any value of the upstream density by scaling densities and pressures by the factor $n_{\text{H}}/50 \text{ cm}^{-3}$ and simultaneously scaling time and lengths by the factor $50 \text{ cm}^{-3}/n_{\text{H}}$.

We start with approximately the steady-state solution for the given cooling law and allow sinusoidal density fluctuations to advect into the shock structure at two mean inflow velocities (150 and 210 km s^{-1}). Numerically, we simply vary with time the upstream boundary condition imposed at the fixed computational boundary. For simplicity, we do not impose numerical flux-limiting techniques in the upstream flow, where these density fluctuations should merely

advect passively.

We choose the two representative mean velocities (150 and 210 km s⁻¹) to represent the range in which we observe the shock instability in the spherical calculations. (Again, these two choices correspond to shock temperatures with different exponents in our piecewise power-law cooling function.) The oscillation period τ implies a characteristic wavelength $L_\tau = 4 \langle v_s \rangle \tau$ for incoming perturbations, where $\langle v_s \rangle$ is the mean relative speed between the shock and the incoming gas. (For the 150 km s⁻¹ case, $L_\tau = 0.1$ pc, and for the 210 km s⁻¹ case, $L_\tau = 0.8$ pc.) One perturbation of this length scale passes through the shock front in approximately the time taken by one cycle of the cooling instability. We choose our fluctuations to have wavelengths λ smaller than and comparable to L_τ , and with amplitudes we label “small” ($\delta n_H / \langle n_H \rangle = 1/14$) and “large” ($\delta n_H / \langle n_H \rangle = 1/2$). (The effect of upstream density perturbations on certain shock oscillations was treated in a recent paper by Walder & Folini [1996]. They simulated the effect of a single sinusoidal density lump on oscillations they identify as less violent than the oscillations we consider here. The results, however, are qualitatively consistent with ours.)

The next several figures show the resulting behavior of v_s in the cases of no, small, and large-amplitude density fluctuations for the various choices of v_s and λ . Figure 7 shows the 150 km s⁻¹, short-wavelength ($\lambda = 0.001$ pc) case; Figure 8, the corresponding moderate-wavelength ($\lambda = 0.02$ pc) case. These calculations use grid size $\Delta x = 10^{-6}$ pc ($\Delta x / L_{\text{cool}}^{\text{ss}} \approx 0.0012$, where $L_{\text{cool}}^{\text{ss}}$ is the steady-state cooling length). Figures 9 and 10 show the two 210 km s⁻¹ cases, with short (0.01 pc) and moderate (0.2 pc) wavelengths respectively; these calculations use $\Delta x = 10^{-5}$ pc ($\Delta x / L_{\text{cool}}^{\text{ss}} \approx 0.0014$). The line segments in each of these figures indicates the fluctuation timescale $\tau = \lambda / \langle v_s \rangle$, where $\langle v_s \rangle$ is 150 km s⁻¹ or 210 km s⁻¹, as appropriate. The passage of these density fluctuations through the shock is reflected in increased, extra variation in shock speed.

Short-wavelength density fluctuations, of small and large amplitude, pass through the shock front in a time small compared with the cooling-instability period and merely vary the shock velocity over the short times required for one wavelength to pass through the shock. The amount of gas that passes through the shock in each cooling-instability period is not changed by these fluctuations, and so the gross features of the cooling-instability fluctuations are unchanged. In the case of the moderate-wavelength fluctuations, however, the amount of gas passing through the shock in each cooling-instability period varies greatly from period to period. This is most pronounced when the density fluctuations have large amplitude, and we see (in Figures 8 and 10) that the evolution of the shock velocity is affected qualitatively. However, we note that in no case is the amplitude of the shock-velocity fluctuations reduced. In the last case, in which there is some qualitative change, the oscillations are increased, not reduced. We conclude that these oscillations should persist in the presence of any upstream density fluctuations.

3. Conclusions

The calculations discussed here show that when the cooling instability is active, the shock velocities of supernova remnants may fluctuate considerably. We see further that reverberations in remnant interiors, consequences of remnants’ complicated births, are unlikely to cause shock-velocity fluctuations of this magnitude.

Density inhomogeneities in the interstellar medium can cause or modify shock-velocity fluctuations. Of course, they may affect the oscillations due to the cooling instability by affecting the mean shock velocity. To have a more direct, large-amplitude effect on oscillations in v_s , however, they must be of quite large amplitude themselves. Our simulations show that to have a substantial qualitative effect on the dynamical cooling oscillations, they must further have length scales comparable to $L_\tau = 4 \langle v_s \rangle \tau$, where τ is the oscillation period. (That is, the shock must traverse this length scale a time comparable to the duration of one oscillation.)

It appears clear that the shocks of many supernova remnants undergo the cooling instability discussed in this paper. The results should be generally correct, although details may be incorrect because of various assumptions: the computations are one-dimensional, the cooling treatment is highly simplified and does not take into account nonequilibrium effects, and the effects of magnetic fields and of radiative transfer are neglected.

In a separate paper (Kimoto & Chernoff 1997) we discuss simulations incorporating a magnetic field oriented transverse to the direction of shock propagation (compression at the shock front tends to align the magnetic field into the plane of the front). These agree with the results of Tóth & Draine (1993), which show that magnetic fields can suppress the global cooling instability by providing a source of non-thermal pressure in cold, dense gas. For cooling laws such as the one we adopt for 130 to 200 km s⁻¹ shocks, however, very large magnetic fields, corresponding to inverse Alfvén Mach numbers $M_A^{-1} = v_A/v_s$ (where the Alfvén speed is $v_A = B/(4\pi\rho)^{1/2}$) in excess of 0.3, would be required to change the qualitative oscillatory behavior. (We note parenthetically that the presence of a magnetic field can change the stability properties at a given shock velocity by changing the shock temperature; this effect may change the velocity at which oscillations cease. For example, we find that a 150 km s⁻¹ shock is stable if the upstream Alfvén velocity is 10 km s⁻¹.) For the cooling law adopted, we conclude that the general picture we have described should hold even with typical magnetic-field strengths.

Raymond et al. (1991) reported some observational evidence for the instability in the Vela supernova remnant. We conclude with a short discussion of considerations for identifying other remnants that may be subject to this instability.

A first requirement for the presence of the instability is for the remnant to be in the radiative phase. Fast radiating remnants may readily be distinguished by the presence of strong optical emission lines (the main sources of the cooling). For example, according to models like those of Cox & Raymond (1985), highly temperature-dependent O III lines identify radiating shocks with

velocities greater than 100 km s^{-1} . In our results, radiating remnants are oscillatory if they have mean shock speeds greater than 120 km s^{-1} , but thus far, most remnants with observed O III lines have inferred shock velocities $\lesssim 100 \text{ km s}^{-1}$ or $> 300 \text{ km s}^{-1}$, outside our range of interest. Hester, Raymond, & Blair (1994) find shocks in the Cygnus Loop remnant with velocities between 130 and 180 km s^{-1} , although they argue that the cooling has not progressed far enough for instabilities to have a significant effect. Of course a precise determination of shock velocities from line emissivities may be hampered by strong differences between the predictions for oscillating cooling columns and for steady-state profiles at the same propagation speed, but nonetheless the strong optical line emission should still be present (Innes et al. 1987).

A different method for determining shock velocities was reported by Koo & Heiles (1991), who made H I 21-cm observations of a collection of northern remnants. Although their observations were hampered by confusion with the Galactic H I background, in many remnants they found high-velocity H I gas. This gas is presumably accelerated by supernova blast waves, and if so it measures the mean remnant expansion speed. Several expansion velocities exceed 120 km s^{-1} and hence may identify objects with shock waves in our range of interest: G 117.4+5.0, HB 21, and OA 184. (The remnant CTA 1 is also listed as having an appreciable expansion velocity, but more recent observations [Pinneault et al. 1993] suggest that the actual velocity is lower.)

Where expansion velocities are not well known, we may identify some candidate objects by seeking the remnant sizes that correspond to the shock velocities of interest. We note from Figure 1 that for a given remnant environment (specified by some value of the ambient density n_{H}) the range of shock radii for which oscillations may be observed is rather limited. If we consider a range of “typical” interstellar densities, however, for example, $0.1 \text{ cm}^{-3} < n_{\text{H}} < 10 \text{ cm}^{-3}$, we find a wide range of shock radii for which the remnants are candidates for oscillations: $10 \text{ pc} \lesssim r_s \lesssim 30 \text{ pc}$ (assuming $E_{51} \approx 1$). Almost half of the 24 Galactic supernova remnants listed by Green (1984, 1988, 1991) as having reasonable distance estimates may lie in this range, and so may have shock velocities that subject them to oscillations. The Vela supernova remnant is selected by this simple criterion; the other objects on this short list are the remnants CTB 37A, CTB 37B, CTB 87, G 320.4–01.2, IC 443, Kes 67, and VRO 42.05.01. We have excluded several with sizes in the range of interest: they are believed to be too young (SN 1006 and RCW 86 [possibly = SN 185]), observations indicate expansion velocities that are too low (CTB 1 [Hailey & Craig 1994]) or too high (W44 [Koo & Heiles 1995]), or they may still be in the adiabatic stage (HB 3 [Leahy et al. 1985]).

We thank Edwin Salpeter and the anonymous referee for useful comments on earlier revisions of this paper.

This research has been carried out at Cornell University with the generous support of the NSF (AST-9119475) and NASA (NAGW-2224) under the LTSA program.

Some computations reported herein were carried out using the resources of the Cornell Theory

Center, which receives major funding from the NSF and New York State, with additional support from ARPA, the National Center for Research Resources at the NIH, IBM Corporation, and other members of the Center’s Corporate Partnership Program.

A. Numerical Methods

The equations of motion for an inviscid one-dimensional cooling gas are

$$\frac{\partial}{\partial t}[r^d \rho] = -\frac{\partial}{\partial r}[r^d \rho v], \quad (\text{A1})$$

$$\frac{\partial}{\partial t}[r^d \rho v] = -\frac{\partial}{\partial r}[r^d \rho v^2] - dr^d \frac{\partial p}{\partial r}, \quad (\text{A2})$$

$$\frac{\partial}{\partial t}[r^d e_{total}] = -\frac{1}{r^d} \frac{\partial}{\partial r}[r^d (e_{total} + p)v] - r^d n_{\text{H}}^2 L(T), \quad (\text{A3})$$

where $n_{\text{H}}^2 f(T)$ gives the rate of energy loss per unit volume, and $d = 0$ for the plane-parallel geometry and $d = 2$ for the spherical geometry. The differencing scheme is based on these equations. We use operator splitting to treat the hydrodynamic and cooling terms separately.

A.1. Hydrodynamics

First we describe the treatment of the hydrodynamics. The pertinent terms on the right-hand sides of equations (A1)–(A3) fall into two classes: (1) the flux terms, expressible as pure spatial derivatives, and (2) the momentum source term $r^2 \partial p / \partial r$ in spherical symmetry. To calculate the numerical fluxes corresponding to the source terms, we use an implementation of flux-corrected transport (FCT) (Zalesak 1979). The FCT method switches between high and low-order numerical fluxes as required to enforce particular variation requirements. For the source term we use simple forward differencing ($u^{n+1} = u^n + \Delta t g(u^n)$, where $g(u)$ specifies the source term as a function of the flow variables).

The FCT flux-calculation method as described by Zalesak (1979) requires calculating high and low-order numerical fluxes. For these we use the Lax-Wendroff and Lax-Friedrichs schemes (Lax & Wendroff 1960; Richtmyer & Morton 1967). The method favors the high-order flux (for accuracy) but switches to the low-order flux where necessary to keep the updated variables within specified bounds. Zalesak recommends choosing these bounds in the following way: Calculate provisional, “diffused” updates \tilde{u}^{n+1} using the low-order fluxes. Set the bounds for the updated values u_j^{n+1} by the minimum and maximum values in the set $\{u_{j-1}^n, u_j^n, u_{j+1}^n, \tilde{u}_{j-1}^{n+1}, \tilde{u}_j^{n+1}, \tilde{u}_{j+1}^{n+1}\}$. We adopt this choice, except that we remove the geometric factors $(r_{j\pm 1}/r_j)^d$ from the values at the neighboring gridpoints.

When applied to inviscid fluid flow, the Lax-Wendroff scheme may develop unphysical features such as oscillations and negative pressures. At low to moderate Mach numbers, the FCT method removes this unphysical behavior. At higher Mach numbers, however, negative pressures can arise near discontinuities and regions of strong gradients. We prevent this by further trying to enforce a lower bound on the internal-energy density (proportional to the pressure).

This internal-energy bounding proceeds in the following complicated way: The updated values

of the flow variables are given by

$$u_j = \tilde{u}_j - \frac{1}{\Delta x}(c_{j+1/2}A_{j+1/2} - c_{j-1/2}A_{j-1/2}), \quad (\text{A4})$$

where \tilde{u}_j is the low-order, “diffused” provisional value and the “antidiffusive fluxes” $A_{j\pm 1/2}$ are defined as the differences between the high- and low-order fluxes. The correction factors $c_{j\pm 1/2}$ lie between 0 and 1 and are determined by the flux-calculation method. (These correction factors are chosen to be functions of the gridpoint but not of the particular quantity being calculated: the same value is chosen for all three equations.) For quantities evolved according to flux and source terms alone, Zalesak gives the algorithm for calculating the correction factors $c_{j\pm 1/2}$.

When written in the form of equation (A4), the updated values can be regarded as functions of the two correction factors: $u_j = u_j(c_{j-1/2}, c_{j+1/2})$. The internal-energy density e_{int} is a known function of the basic flow variables u_j , and so we likewise regard it as a function of the two correction factors.

If the partial derivatives $\partial e_{\text{int}}/\partial c_{j\pm 1/2}$ have the same sign, then we find \tilde{c} , the largest allowed value of c between 0 and 1 such that $e_{\text{int}}(\tilde{c}, \tilde{c})$ is greater than the imposed minimum value. Then we test this value of \tilde{c} by evaluating $e_{\text{int}}(\tilde{c}, 0)$ and $e_{\text{int}}(0, \tilde{c})$. In the (unlikely) event that either of these is disallowed (i.e., less than the minimum acceptable value), we reduce \tilde{c} so that these two test quantities lie in the accepted range.

Next, consider the other case, in which only one of the two partial derivatives is negative. The simulations described in this paper employ the following method: for specificity, let the negative partial derivative be $\partial e_{\text{int}}/\partial c_{j-1/2}$. We find $\tilde{c}_{j-1/2}$, the largest value of $c_{j-1/2}$ between 0 and 1 such that $e_{\text{int}}(\tilde{c}_{j-1/2}, 0)$ lies in the acceptable range. Then we test this value of $\tilde{c}_{j-1/2}$ by evaluating $e_{\text{int}}(\tilde{c}_{j-1/2}, 1)$. In the (unlikely) event that it falls outside the acceptable range, we reduce $\tilde{c}_{j-1/2}$ so that this test quantity falls within the acceptable range.

(In other simulations, such as those incorporating a one-dimensional magnetic field—for example, those described in Kimoto & Chernoff [1997]—we find that the above method does not prevent negative internal energies, and so we use the following alternative method: We find the two quantities $\bar{c}_{j\pm 1/2}$, the largest values of $c_{j\pm 1/2}$ between 0 and 1 such that $e_{\text{int}}(\bar{c}_{j-1/2}, 0)$ and $e_{\text{int}}(0, \bar{c}_{j+1/2})$ lie in the acceptable range. Then we test these values by evaluating $e_{\text{int}}(\bar{c}_{j-1/2}, \bar{c}_{j+1/2})$. In the event that it lies outside the acceptable range, we use instead the values of $\tilde{c}_{j\pm 1/2}$, determined so that $e_{\text{int}}(\tilde{c}_{j-1/2}, \bar{c}_{j+1/2})$ and $e_{\text{int}}(\bar{c}_{j-1/2}, \tilde{c}_{j+1/2})$ are acceptable.)

This prescription calculates values of the correction factors $c_{j\pm 1/2}$ that, in the vast majority of cases, ensure that the internal-energy density e_{int} remains above the imposed minimum value. (In all of the simulations discussed in this paper, it ensures that the internal-energy density remains positive.) We use the smallest, most conservative value of the correction factors, taken from this prescription and the standard FCT method.

A.2. Cooling

As noted in the previous subsection, we use operator splitting to treat hydrodynamics and cooling separately. We use the first-order-accurate semi-implicit Euler method to perform the update. We fit the radiative cooling law of Raymond et al. (1976) by a piecewise set of power laws. (These power laws are calculated to fit the set of values enumerated below.) To turn the cooling off at low temperatures $T \lesssim 2 \times 10^4$ K, we multiply the power-law fit by a function

$$\mathcal{T}(T) = \frac{1}{2} \left[1 + \tanh \left(\frac{T - 1.75 \times 10^4 \text{ K}}{860 \text{ K}} \right) \right]. \quad (\text{A5})$$

T (K)	cooling rate (ergs cm ³ s ⁻¹)
1.0×10^4	4.0
1.5×10^4	22.0
3.2×10^4	14.0
1.0×10^5	68.0
2.5×10^5	15.0
5.0×10^5	15.0
2.0×10^6	13.0

A.3. Multigrid

In order to calculate regions of particular interest accurately (i.e., near the shock and the dense shell), we use a hierarchy of grids with different grid sizes. Berger & Colella (1989, hereafter BC) describe a method for solving systems of conservation laws on locally refined grids. (They describe both the method for working with a hierarchy of grids and an algorithm to determine where local mesh refinement is required. We employ only the former ideas.)

The BC method integrates local high-resolution calculations nested within larger, lower-resolution calculations. It maintains the global conservation laws, as required to ensure the correct evolution of discontinuities such as shocks. We borrow their method for maintaining multiple grids.

Within the BC framework one must often interpolate values from coarse grids onto fine grids, for example, when introducing new fine grids or when calculating values at the boundary of existing fine grids. (The inverse process, transferring values from fine to coarse grids, must be done via spatial averaging in order to maintain the global conservation laws). We adopt the interpolation method used within the piecewise-parabolic method (PPM) of Colella & Woodward (1984; Woodward 1986). This method produces interpolating parabolas from gridpoint values. We enforce a monotonicity constraint, as described by Colella & Woodward, but no more complicated modifications (such as their discontinuity detection).

The PPM interpolation method ensures that the values of conserved quantities on fine grids are completely consistent with their values on the corresponding coarse grids. (That is, the transfer of values back, from fine to coarse grids, yields the same coarse-grid values.) The method, however, occasionally yields unphysical values for fine-grid quantities. Once again, the problem is usually negative pressures. In the calculations we made for this paper, such calculated unphysical values arose only in the region just outside the boundaries of fine grids. (The use of values just outside fine-grid boundaries is the way that fine-grid boundary conditions are enforced in the BC formalism.) When these unphysical values arise, we replace the interpolated quantities by physically allowed values, obtained by interpolating the “primitive” variables ρ , v , and p directly. (We further require that the interpolating parabolas for ρ and p remain positive.) Because these are not the conservation-law variables, we lose “consistency” (in the sense defined above) between coarse and fine grids. This does not affect the treatment of the global conservation laws, however, because these values are used merely for boundary conditions, and do not lie within the fine grids proper.

BC give a sophisticated algorithm for determining where to place refined grids, but for our purposes these are not required. In our simulations the region most in need of high resolution is always the cooling region just behind the main shock. Within this region, most important are its two edges, namely (1) the shock itself and (2) the region of rapid cooling and strong density gradient. It is computationally simple to determine the location of both these features by searching inward from the upstream boundary. (We locate the shock by its characteristic pressure jump, and we locate the steep density gradient by some large value of the mass density that it must encompass. Of course, the latter criterion does not apply before the dense shell forms.) The subgrid for each refined region has a specified size, and on each time step a grid’s subgrids may be translated to follow the motion of the appropriate features.

Refinement algorithms (such as presented by BC) may determine how much refinement should be applied, but we do not use these methods, either. For our purposes it suffices to choose a fixed grid size for each refined level within a computation. It is still possible for the program user to change the refinement of levels by pausing the evolution program and modifying the representation of the flow, but naturally it is practical to do this only at isolated times. In the spherically symmetric computations the mean cooling length decreases steadily as the shock velocity (and hence the shock temperature) decreases; as it shrinks such intervention to decrease the grid size can be necessary in order to maintain sufficient resolution on the region.

A.4. Time step

For each time step of the coarsest grid in the grid hierarchy (which corresponds to multiple time steps for its subgrids), we calculate a new value of the time step Δt . For hydrodynamic

stability we obey the Courant-Friedrichs-Lewy condition (Richtmyer & Morton 1967) by calculating

$$(\Delta t)_{\text{CFL}} = 0.9 \min_{\text{grid}} \frac{\Delta r}{|v| + c} \quad (\text{A6})$$

on the coarsest grid *only*. For accuracy of the cooling treatment, we calculate

$$(\Delta t)_{\text{cool}} = 0.1 \min_{\text{grid}} \frac{e_{\text{int}}}{n_{\text{H}}^2 L(T)}, \quad (\text{A7})$$

on all parts of *each* grid that is not covered by another, more highly refined grid. The time step used, then, is $\Delta t = \min[(\Delta t)_{\text{CFL}}, (\Delta t)_{\text{cool}}]$.

A.5. Boundary conditions

We enforce several types of boundary conditions. All are straightforward to implement numerically. Our computational framework requires specification of input fluxes entering the edge zones so that the recipe for their updates is the same as that for interior zones. The enforcement of boundary conditions, then, requires methods for determining fluxes entering the computational region from the outside.

First we describe the upstream (ISM) boundary condition. In this region we know exactly what values the flow variables should take at positions off the computational region. Thus we can define several (phantom) zones off the edge of the computational region. The edge fluxes can then be computed from these and the “real” zones inside the computational region, just as the fluxes in the interior are computed.

Next we describe the Sedov-Taylor interior boundary condition. Here we are given particular values to impose at a particular position. In this case we simply define the flux entering that zone from the (phantom) exterior of the computational region to be whatever value is required so that the updated values in that zone take on the desired values.

Last we describe the perfectly reflecting boundary condition. We impose this condition at the position of the gridpoint itself. As in the previous situation, we choose the (phantom) momentum flux entering the edge zone such that the velocity there vanishes. For the other phantom fluxes, we set them equal in magnitude but opposite in sign to the fluxes entering the zone from the interior of the computational region, since that is equivalent to having the zone divided in half by a wall (which of course allows no fluxes through it).

REFERENCES

- Berger, M. J., & Colella, P. 1989, *J. Comput. Phys.*, 82, 64 (BC)
- Bertschinger, E. *ApJ*, 304, 154
- Chevalier, R. A. 1977, *ARA&A*, 15, 175
- Chevalier, R. A., & Blondin, J. M. 1995, *ApJ*, 444, 312
- Chevalier, R. A., Blondin, J. M., & Emmering, R. T. 1992, *ApJ*, 392, 118
- Chevalier, R. A., & Imamura, J. N. 1982, *ApJ*, 261, 543
- Colella, P., & Woodward, P. R. 1984, *J. Comput. Phys.*, 54, 174
- Cioffi, D. F., McKee, C. F. & Bertschinger, E. 1988, *ApJ*, 334, 252
- Cox, D. P., & Raymond, J. C. 1985, *ApJ*, 298, 651
- Draine, B. T., & McKee, C. F. 1993, *ARA&A*, 31, 373
- Gaetz, T. J., Edgar, R. J., & Chevalier, R. A. 1988, *ApJ*, 329, 927
- Goodman, J. 1990, *ApJ*, 358, 214
- Green, D. A. 1984, *MNRAS*, 209, 449
- Green, D. A. 1988, *Ap&SS*, 148, 3
- Green, D. A. 1991, *PASP*, 103, 209
- Hailey, C. J., & Craig, W. W. 1994, *ApJ*, 434, 635
- Hester, J. J., Raymond, J. C., & Blair, W. P. 1994, *ApJ*, 420, 721
- Imamura, J. N., Wolff, M. T., & Durisen, R. H. 1984, *ApJ*, 276, 667
- Innes, D. E., Giddings, J. R., & Falle, S. A. E. G. 1987, *MNRAS*, 226, 67
- Kimoto, P. A., & Chernoff, D. F. 1995, *ApJS*, 96, 627
- Kimoto, P. A., & Chernoff, D. F. 1997, *ApJ*, in press
- Koo, B., & Heiles, C. 1991, *ApJ*, 382, 204
- Koo, B., & Heiles, C. 1995, *ApJ*, 442, 679
- Langer, S. H., Chanmugam, G., & Shaviv, G. 1981, *ApJ*, 245, L23
- Lax, P., & Wendroff, B. 1960, *Comm. Pure Appl. Math.*, 13, 217

- Leahy, D. A., Venkatesan, D., Long, K. S., & Naranan, S. 1985, *ApJ*, 294, 183.
- Luo, D., & Chevalier, R. A. 1994, *ApJ*, 435, 815
- Pinneault, S., Landecker, T. L., Madore, B., & Gaumont-Guay, S. 1993, *AJ*, 105, 1060
- Raymond, J. C., Cox, D. P., & Smith, B. W. 1976, *ApJ*, 204, 290
- Raymond, J. C., Wallenstein, G., & Balick, B. 1991, *ApJ*, 383, 226
- Richtmyer, R. D., & Morton, K. W. 1967, *Difference Methods for Initial-Value Problems* (2nd ed., New York: Interscience)
- Sedov, L. I. 1959, *Similarity and Dimensional Methods in Mechanics* (New York: Academic)
- Shull, J. M., & McKee, C. F. 1979, *ApJ*, 227, 131
- Tóth, G., & Draine, B. T. 1993, *ApJ*, 413, 176
- Vishniac, E. 1983, *ApJ*, 274, 152
- Walder, R., & Folini, D. 1996, *A&A*, 315, 265
- Woodward, P. R., in *Astrophysical Radiation Hydrodynamics*, ed. K.-H. A. Winkler & M. L. Norman (Dordrecht: D. Reidel), 245
- Zalesak, S. T. 1979, *J. Comput. Phys.*, 31, 335

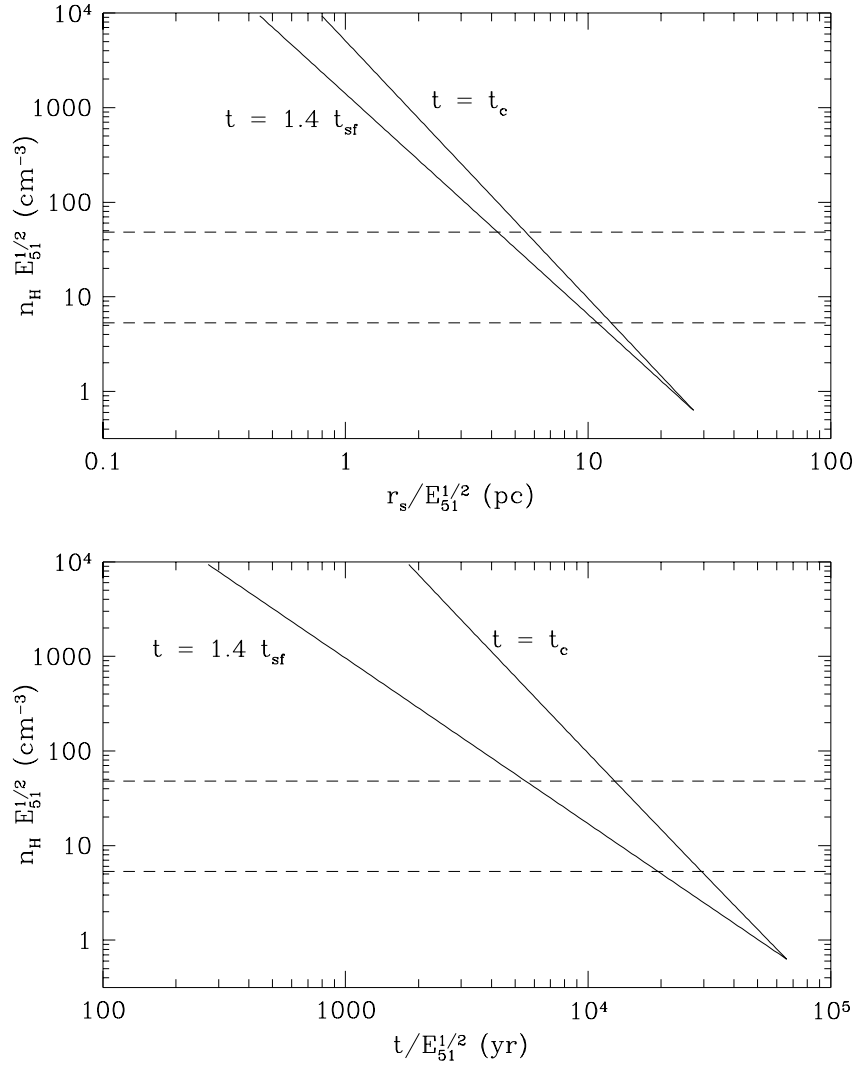


Fig. 1.— The estimated shock radii and time period for shock oscillations as functions of interstellar-medium density. The two solid lines delimit the time interval. (Here we assume that the oscillations end when the shock velocity reaches 130 km s^{-1} .) The two horizontal, dotted lines represent the two cases simulated in which we find oscillations ($n_{\text{H}} = 5.5 \text{ cm}^{-3}$ and 50 cm^{-3} , both with $E_{51} = 0.931$).

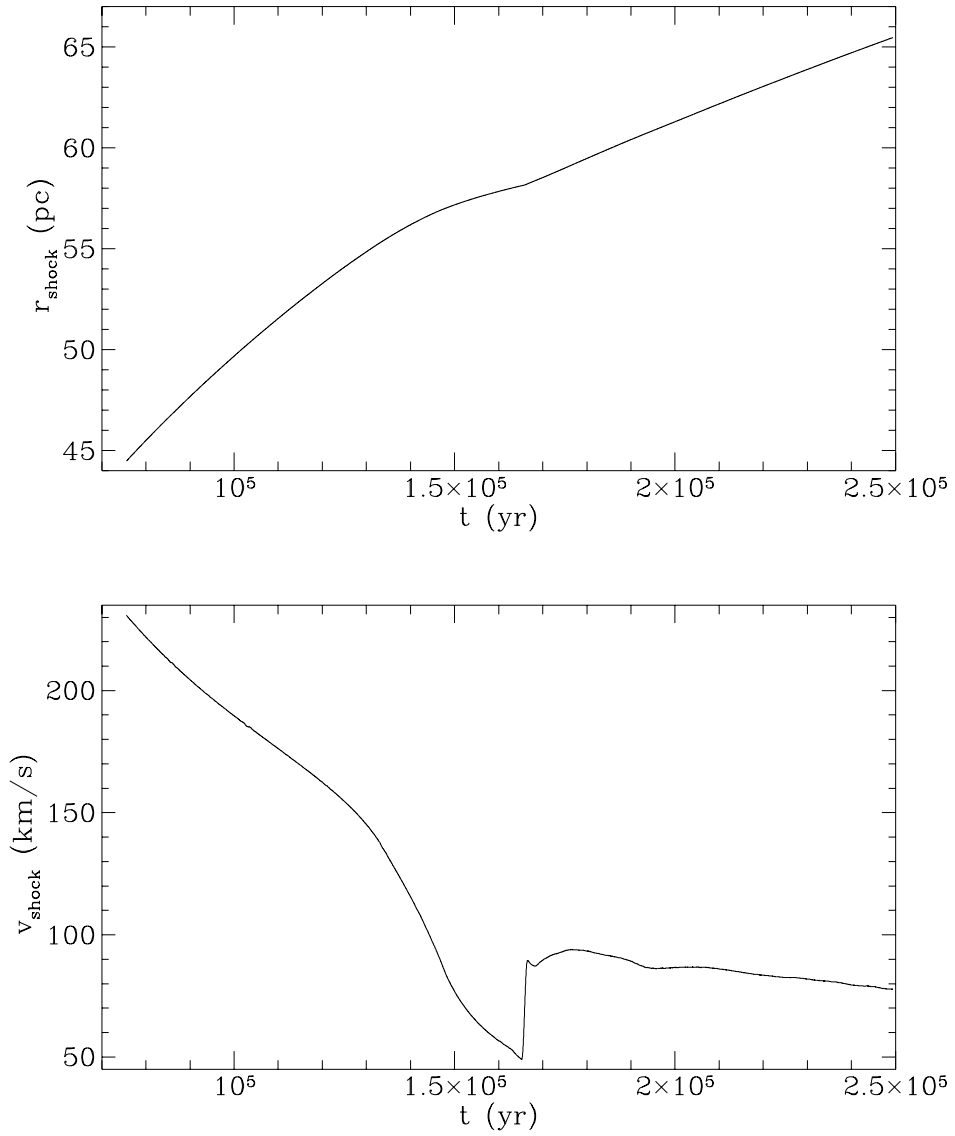


Fig. 2.— Shock position and velocity as a function of remnant age for an interstellar-medium density $n_{\text{H}} = 0.1 \text{ cm}^{-3}$.

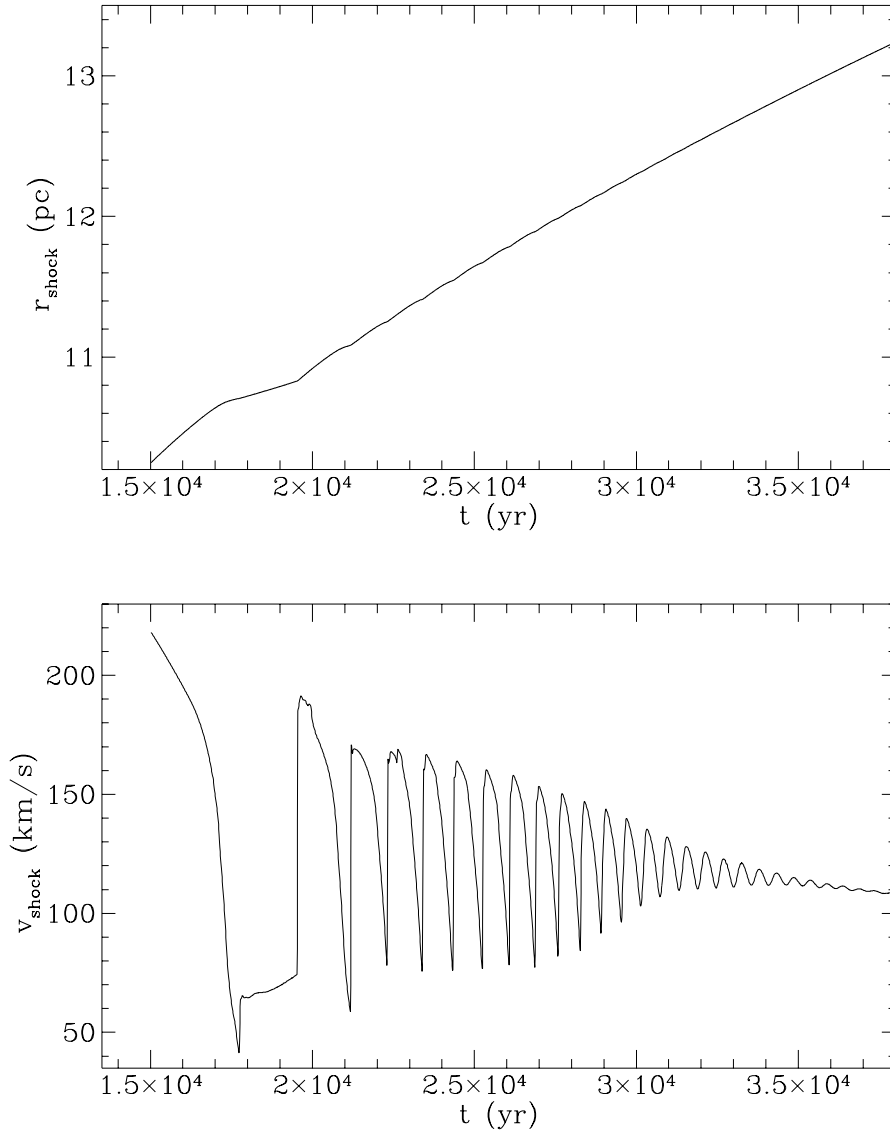


Fig. 3.— Shock position and velocity for ISM density $n_{\text{H}} = 5.5 \text{ cm}^{-3}$.

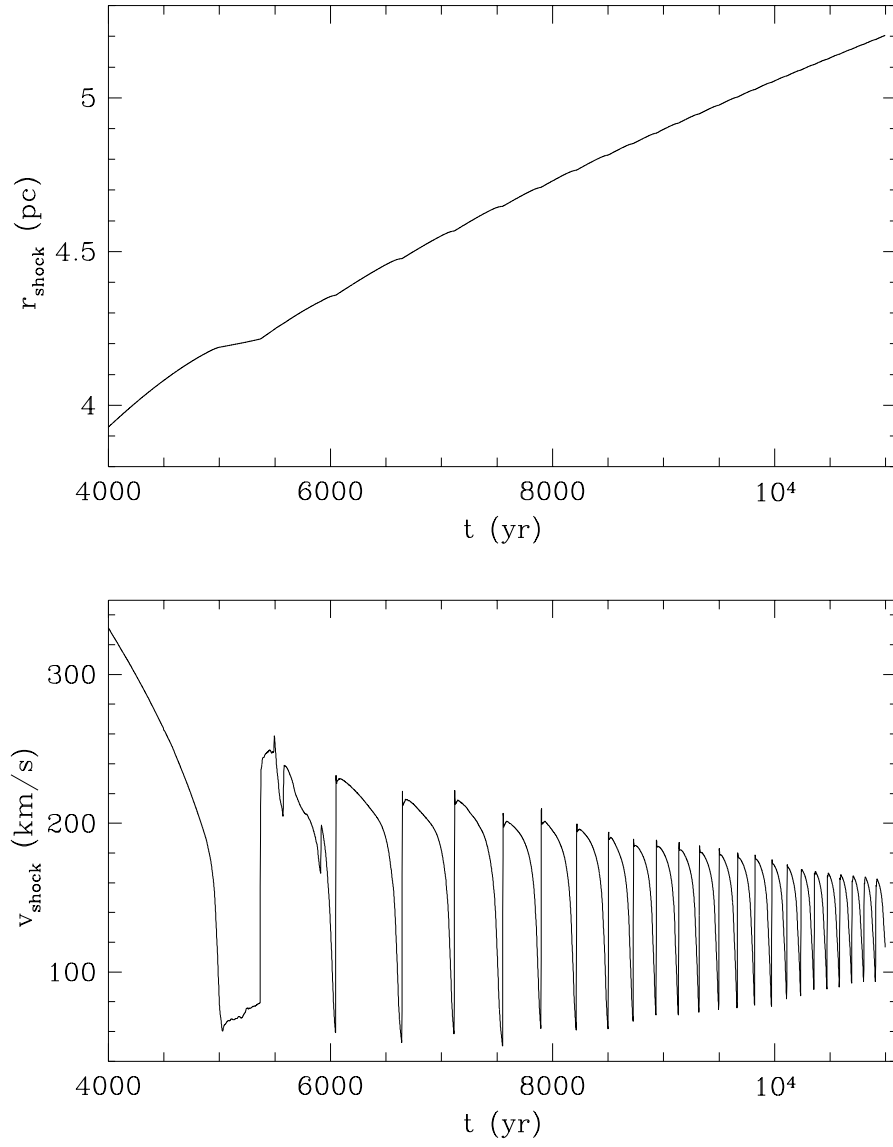


Fig. 4.— Shock position and velocity for ISM density $n_{\text{H}} = 50 \text{ cm}^{-3}$.

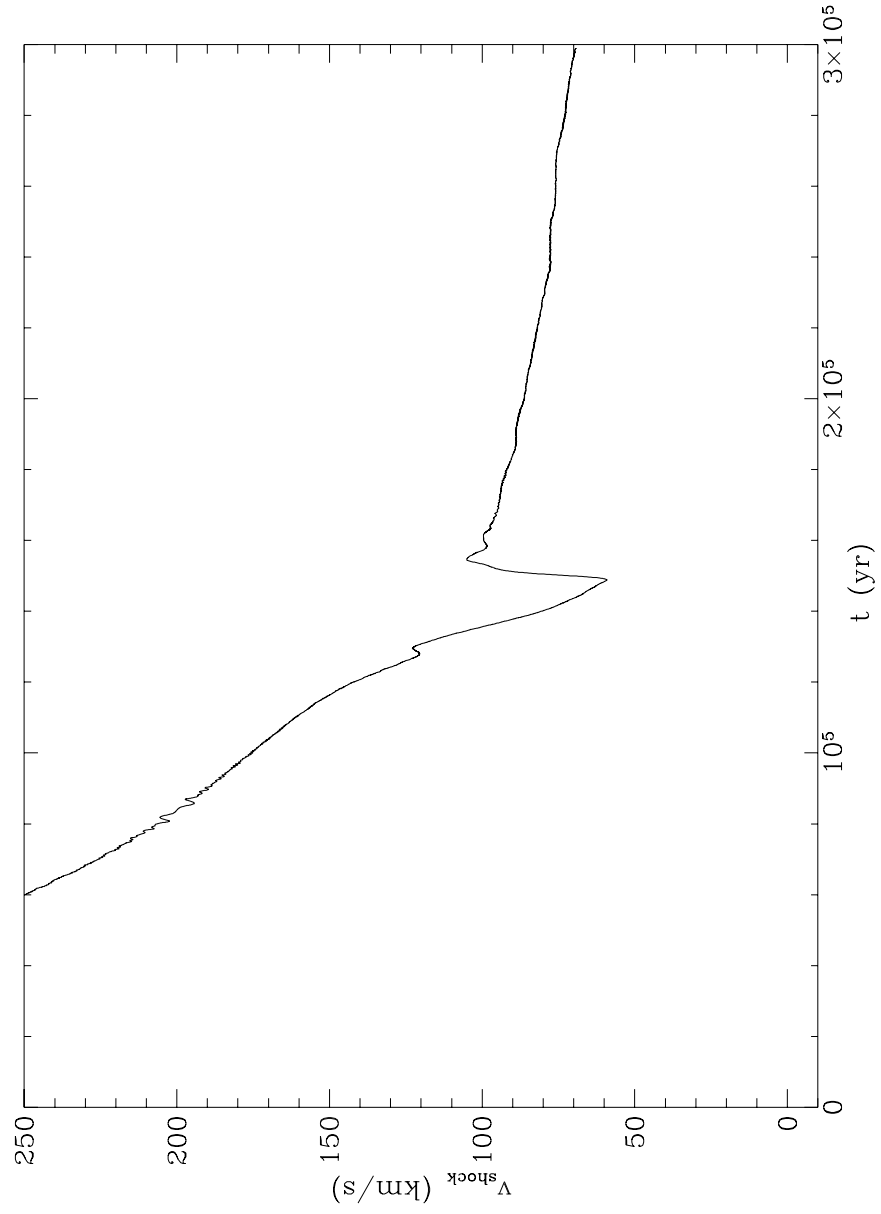


Fig. 5.— Shock velocity for ISM density $n_{\text{H}} = 0.1$ for calculation using hard-sphere interior boundary condition.

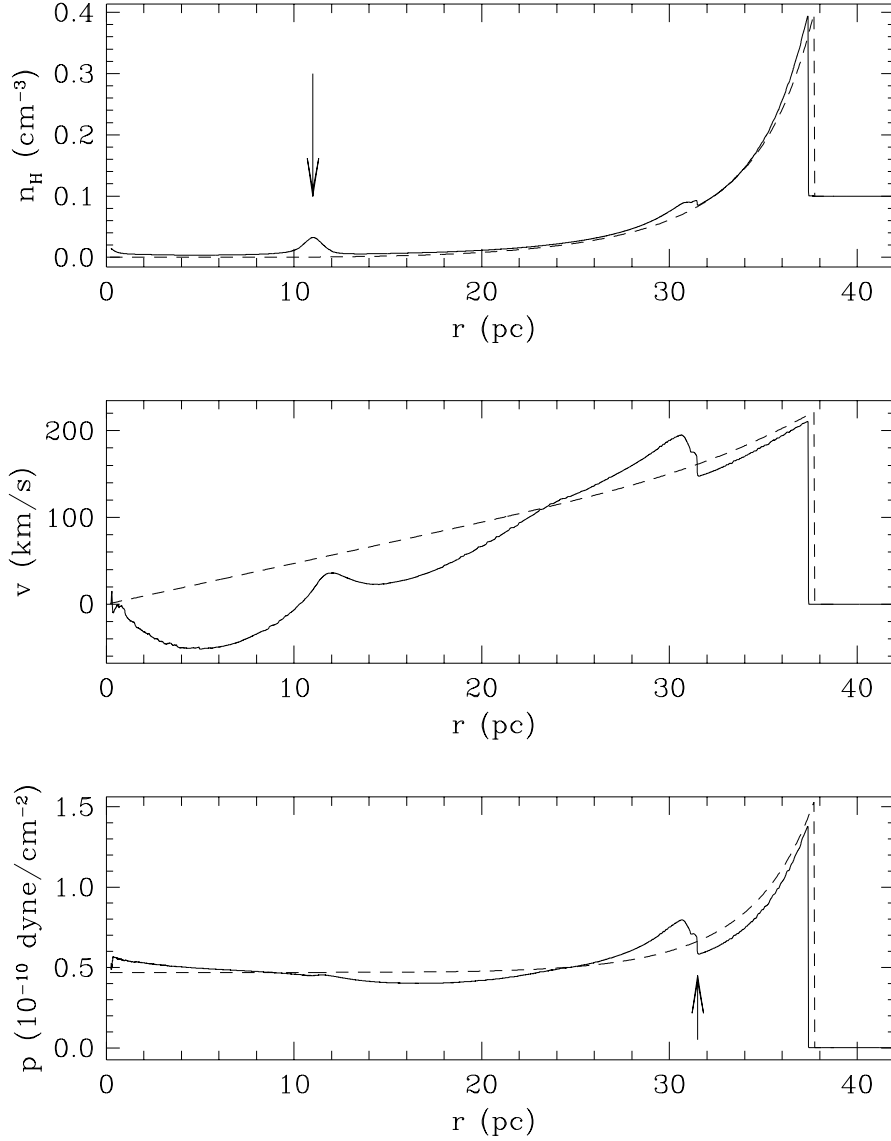


Fig. 6.— Density, velocity, and pressure at $t = 5 \times 10^4$ yr with ISM density $n_{\text{H}} = 0.1 \text{ cm}^{-3}$ and hard-sphere interior boundary condition. The arrow in the top panel points out a density enhancement, a remnant of the initial conditions; the arrow in the bottom panel points out a secondary shock. The Sedov-Taylor similarity solution at this time is given with dotted lines.

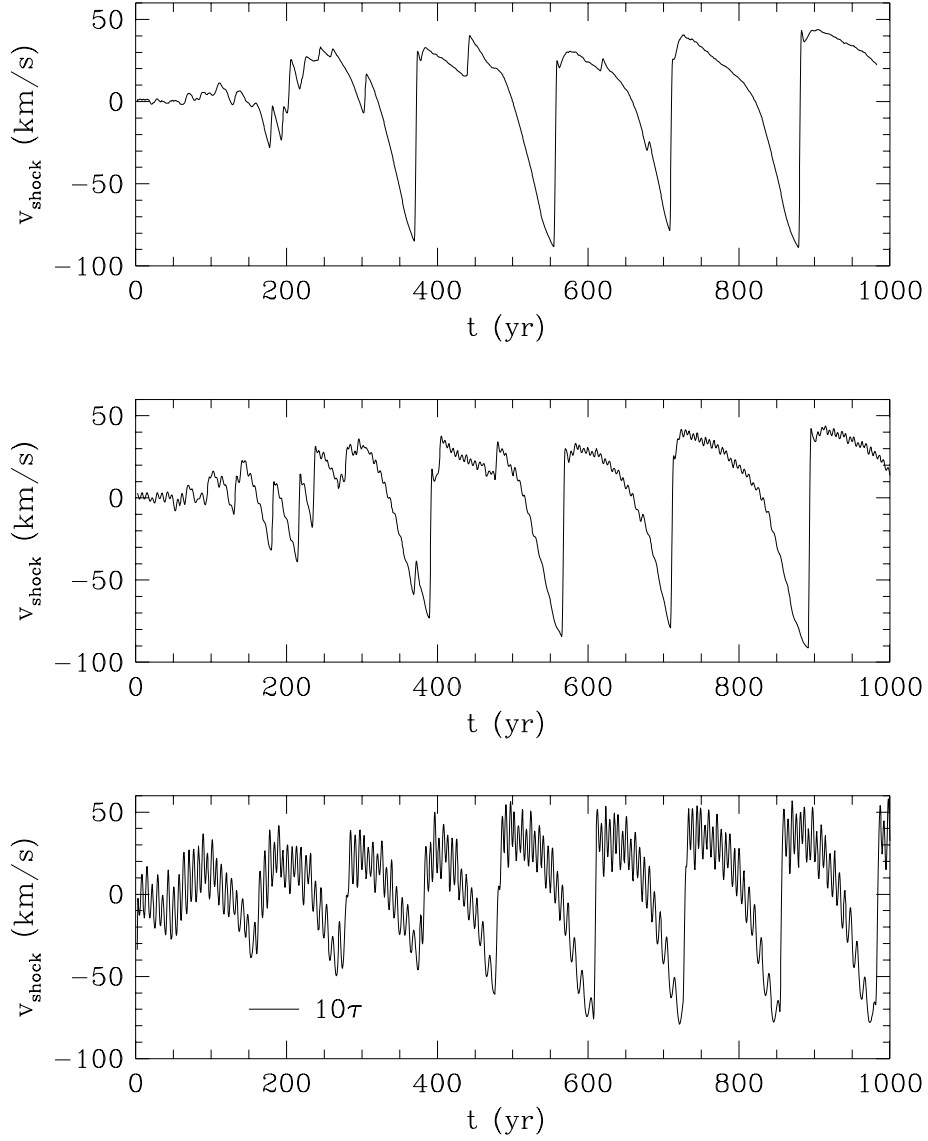


Fig. 7.— Evolution of shock velocity for a shock moving with mean velocity 150 km s^{-1} . We show the effect of short-wavelength upstream density perturbations by comparing the cases of (top) no, (middle) small, and (bottom) large-amplitude fluctuations. The line segment in the bottom panel indicates an interval 10 times the fluctuation timescale τ .

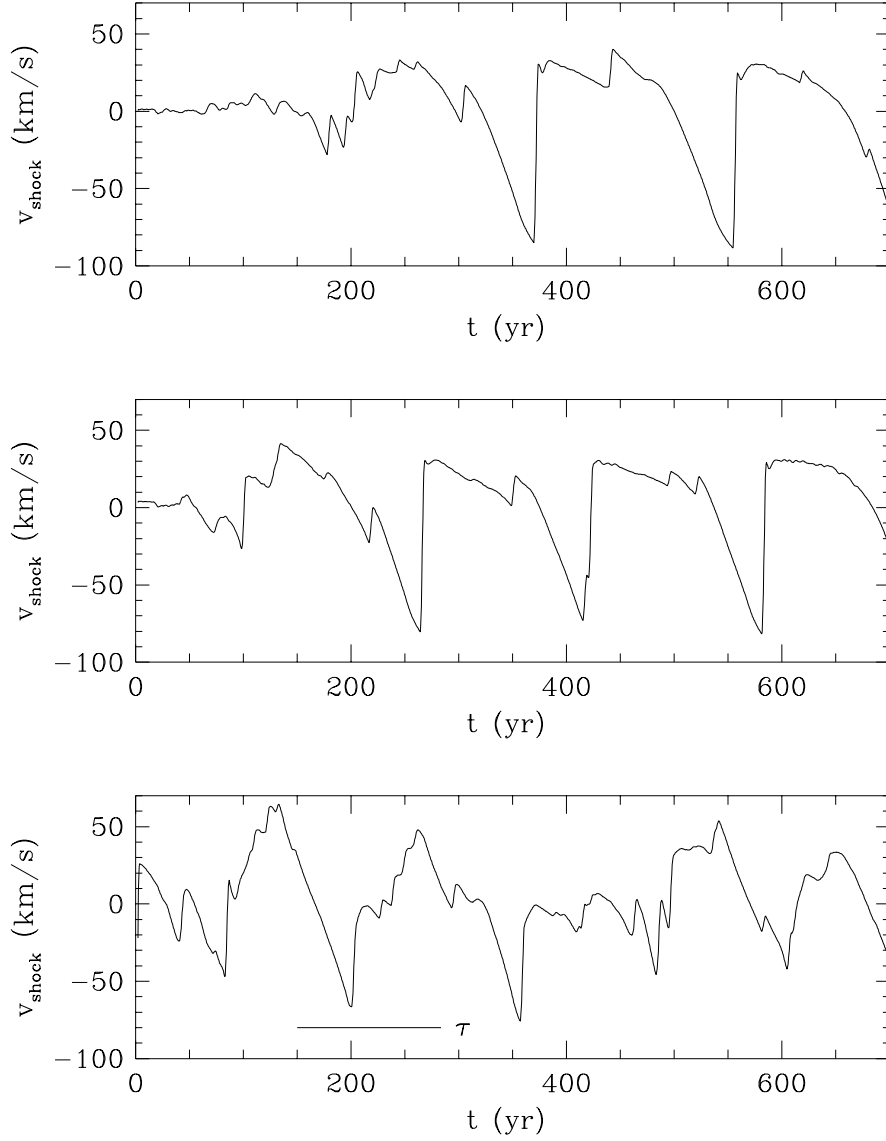


Fig. 8.— Evolution of shock velocity for a shock moving with mean velocity 150 km s^{-1} perturbed by moderate-wavelength upstream density fluctuations. We show the cases of (top) no, (middle) small, and (bottom) large-amplitude fluctuations. The line segment in the bottom panel indicates the fluctuation timescale τ .

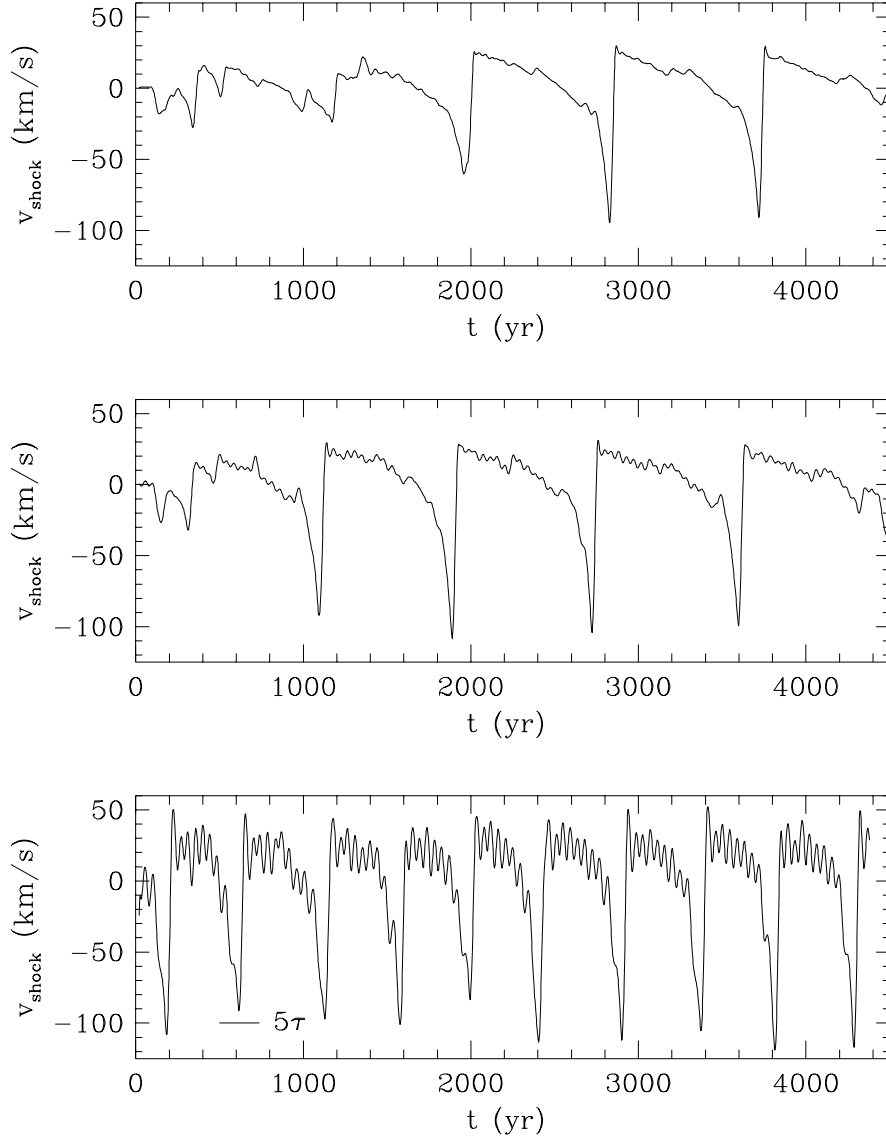


Fig. 9.— Evolution of shock velocity for a shock moving with mean velocity 210 km s^{-1} perturbed by short-wavelength upstream density fluctuations. We show the cases of (top) no, (middle) small, and (bottom) large-amplitude fluctuations. The line segment in the bottom panel indicates a time interval five times the fluctuation timescale τ .

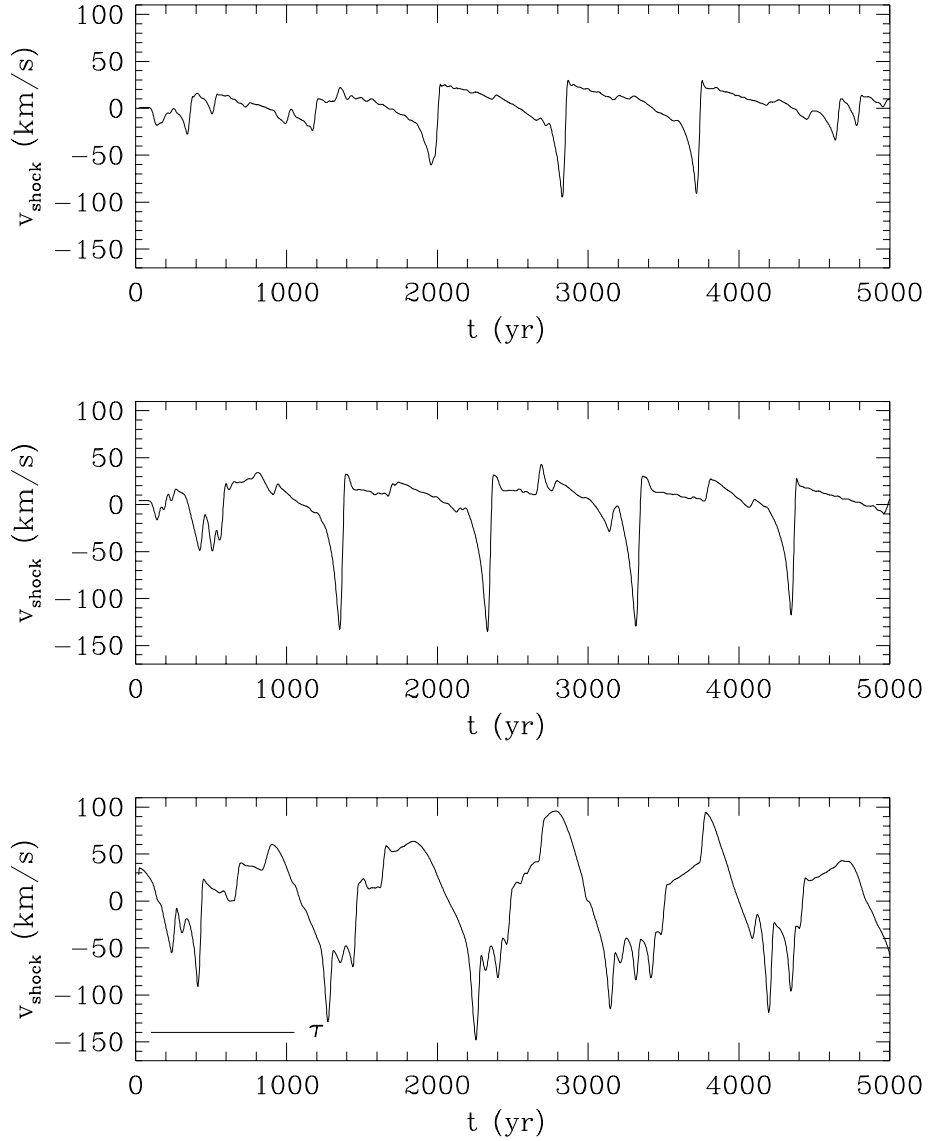


Fig. 10.— Evolution of shock velocity for a shock moving with mean velocity 210 km s^{-1} perturbed by moderate-wavelength upstream density fluctuations. We show the cases of (top) no, (middle) small, and (bottom) large-amplitude fluctuations. The line segment in the bottom panel indicates the fluctuation timescale τ .